Research Article Vol. 5, No. 8 / August 2018 / Optica 924

Computational complex optical field imaging using a designed metasurface diffuser

Hyounghan Kwon, Ehsan Arbabi, Seyedeh Mahsa Kamali, MohammadSadegh Faraji-Dana, and Andrei Faraon*

T. J. Watson Laboratory of Applied Physics and Kavli Nanoscience Institute, California Institute of Technology, 1200 E. California Blvd., Pasadena, California 91125, USA
**Corresponding author: faraon@caltech.edu*

Received 27 April 2018; revised 27 June 2018; accepted 3 July 2018 (Doc. ID 330497); published 30 July 2018

Various speckle-based computational imaging techniques that exploit the ability of scattering media to transfer hidden information into the speckle pattern have recently been demonstrated. Current implementations suffer from several drawbacks associated with the use of conventional scattering media (CSM), such as their time-consuming characterization, instability with time, and limited memory-effect range. Here we show that by using a random dielectric metasurface diffuser (MD) with known scattering properties, many of these issues can be addressed. We experimentally demonstrate an imaging system with the ability to retrieve complex field values using a MD and the speckle-correlation scattering matrix method. We explore the mathematical properties of the MD transmission matrix such as its correlation and singular value spectrum to expand the understanding about both MDs and the speckle-correlation scattering matrix approach. In addition to a large noise tolerance, reliable reproducibility, and robustness against misalignments, using the MD allows us to substitute the laborious experimental characterization procedure of the CSM with a simple simulation process. Moreover, dielectric MDs with identical scattering properties can easily be mass-produced, thus enabling real-world applications. Representing a bridge between metasurface optics and speckle-based computational imaging, this work paves the way to extending the potentials of diverse speckle-based computational imaging methods for various applications such as biomedical imaging, holography, and optical encryption.

OCIS codes: (050.6624) Subwavelength structures; (110.6880) Three-dimensional image acquisition; (110.1758) Computational imaging.

https://doi.org/10.1364/OPTICA.5.000924

1. INTRODUCTION

Imaging through scattering media is one of the most challenging problems in optics, as the passage of coherent light through scatterers leads to complicated speckle patterns. Various methods for imaging objects through scattering media, such as optical coherence tomography [1], wavefront engineering [2], speckle correlation based on the memory effect [3,4], and the transmission matrix [5], have been reported.

In the past few years, various computational techniques that retrieve hidden information from changes in complicated speckle patterns have been proposed [6–22]. These speckle-based computational imaging techniques, which utilize the benefits of scattering instead of considering it an obstacle, have unique merits in capturing various types of hidden information that are otherwise challenging to obtain with conventional imaging systems, or require a higher degree of complexity in the optical system. For example, progress has been made toward developing diverse speckle-based computational imaging techniques for retrieving depth or three-dimensional information. These techniques include phase-space measurements [6,7], speckle holography with a reference point source [8], compressed sensing techniques with speckle patterns [9,10], deconvolution with the manipulated point spread function based on the memory effect [11], the speckle-correlation scattering matrix (SSM) [12,13], and wavefront sensing with the Demon algorithm [14]. Based on the spectral decorrelation characteristics of the speckle pattern, various methods to retrieve spectral information have also been explored [15–18]. Moreover, speckle-based computational imaging methods allow for retrieval of more diverse information about the light, such as its polarization [19] or orbital angular momentum [20], and also can lead to retrieval of images with enhanced resolution [21,22].

In particular, the SSM method has recently been proposed to enable complex field measurements without a reference signal [12,13,19,20]. However, the previous works focus only on the optical methods or computational aspects, leaving out the scattering medium as an integral part of the scheme. Similar to other scattering-based techniques, the use of conventional scattering media (CSM) has many drawbacks that significantly limit the

potential of this technique for real applications. For example, the instability of the optical properties [23], the fluctuation in transmittance of diffusive CSM [24], and the trade-off between memory-effect range and maximum scattering angular range [25] could be critical drawbacks from a practical point of view. Most important, the cumbersome experimental characterization procedure that should be individually repeated for every scattering medium is an important barrier that will be extremely challenging to overcome if systems employing such techniques are to be mass-produced and commercialized.

Optical metasurfaces, composed of nano-scatterers or meta-atoms, can manipulate the phase, amplitude, and polarization of light at subwavelength scales [26–30]. Various conventional optical components [31–35] as well as newer optical devices [36,37] have already been demonstrated using metasurfaces. In addition, concepts of computational optics with metasurfaces were recently proposed in the context of full-color imaging [38] and optical encryption [39]. Moreover, several investigations about the statistical or physical properties of random metasurfaces, such as the far-field response [40,41] or the random Rashba effect [42], have been reported. Recently, the concept of the metasurface diffuser (MD) was also proposed for wavefront control with a spatial light modulator, demonstrating wide field of view (FOV) and high-resolution bio-imaging [25]. However, the investigation focused on wavefront shaping rather than computational imaging based on the properties of the speckle patterns.

Here we propose the use of designed MDs that replace CSMs for the purpose of complex field and three-dimensional imaging. The performance of the complex field imager is demonstrated in both simulation and experiment. In particular, measurements of amplitude samples and holographic imaging with numerical back-propagation verify the MD's capability for complex field retrieval with real objects. In addition, several benefits of the MD such as replacing the laborious characterization procedure of the CSM with a significantly simpler simulation process, reproducibility, stability, high noise tolerance, and robustness against misalignments are also demonstrated and discussed. Moreover, we explore the mathematical properties of the transmission matrix (**T**), such as the correlation between its columns and the randomness of its entries indicated by the singular value spectrum. These properties give important insight into the optical properties of the MD as a scattering medium and clarify the required operating conditions of the SSM method.

2. METASURFACE DIFFUSER DESIGN

Figure 1 schematically illustrates the concept of the MD-based complex field imager. Light from the object is scattered by the MD and leads to a speckle pattern that is captured by an image sensor. Using the computed **T** matrix of the designed MD and the captured intensity of the speckle pattern, the complex fields of the object can be retrieved. The MD works as a cross-polarized random phased array that scatters light with greater efficiency than amplitude masks, which are widely used in compressed sensing schemes [43–45]. In other words, the MD is designed to operate as a half-wave plate (HWP), and at the same time to scatter light uniformly.

The MD, schematically shown in Fig. 2(a), is composed of high-contrast birefringent amorphous silicon (α-Si) meta-atoms [46]. The meta-atoms are 652 nm tall and rest on a square lattice with a lattice constant of 500 nm. The design wavelength is

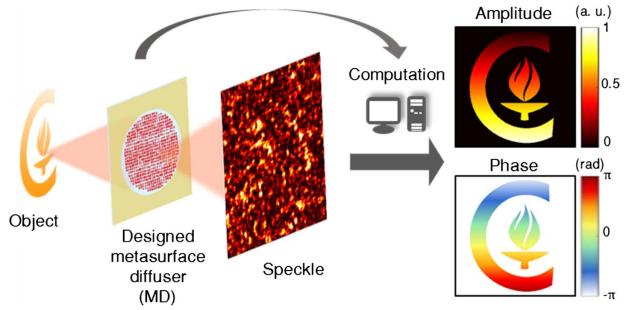

Fig. 1. Schematic illustration of computational complex field retrieval using a designed MD. Light from the object is scattered by the metasurface, resulting in a speckle pattern. The known phase profile of the MD is then used in a computational procedure based on the SSM method to retrieve the complex fields of the object from the captured speckle pattern.

850 nm. The meta-atoms shown in Fig. 2(b) have rectangular cross sections with side lengths D_x and D_y along the x and y axes, respectively. With proper design, the meta-atoms provide independent 2π phase coverage for x- and y-polarized light. The meta-atom side lengths versus the phase delays for two orthogonal polarizations (ϕ_x and ϕ_y) are plotted in Fig. 2(c) (see Section S1 and Fig. S1 of Supplement 1 for details of the simulation results, design, and fabrication).

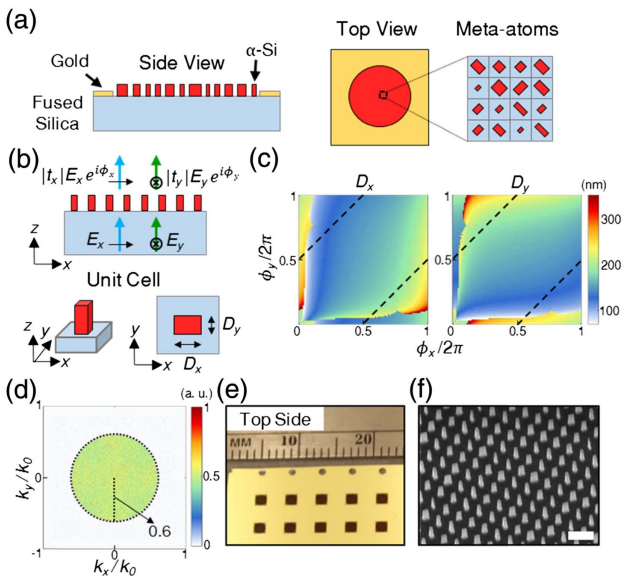

Fig. 2. MD structure and design. (a) Schematic illustration of the side and top views of the MD. The α-Si meta-atoms are arranged in a square lattice on a fused silica substrate. A gold layer is deposited to block the light outside the diffuser aperture. (b) Schematics of a uniform array (top) and a unit cell of the metasurface (bottom), showing the parameter definitions. The transmission phase of the two orthogonal polarizations can be manipulated using the meta-atoms. (c) Calculated in-plane dimensions of the meta-atoms (D_x and D_y) as functions of the required transmission phases for x- and y-polarized light (ϕ_x and ϕ_y, respectively). The black dashed lines show the meta-atoms that work as a half-wave plate (i.e., $|\phi_x - \phi_y| = \pi$). (d) Calculated amplitude of the Fourier transform of the MD's phase mask. (e) Optical image of the fabricated MD array. (f) Bird's-eye-view scanning electron microscope image of a portion of the metasurface. The scale bar is 1 μm.

To suppress the power of the unscattered light after the MD (which is inevitable due to the finite scattering efficiency and fabrication imperfections), we designed and used the MD in a cross-polarized configuration. To this end, each meta-atom operates as a HWP whose optical axis makes a 45 deg angle with the x and y directions [Fig. 2(a), right]. As a result, the x-polarized input light will be scattered to the y-polarized output. The unscattered light is then rejected using a linear polarizer. We should note here that this is an important additional benefit of the capabilities of MDs, not achievable with CSM.

In the MD design process, the data in Fig. 2(c) act as a lookup table, with the dashed black lines corresponding to the HWP meta-atoms. Similar to other local dielectric metasurfaces, the MD acts as a phase mask characterized by a two-dimensional complex transmission function. In order for the MD to scatter light isotropically, we designed the phase mask to have uniform amplitude in the Fourier domain. As shown in the simulation results in Fig. 2(d), the numerical aperture of the MD is set to 0.6, which means that it scatters light to a maximum angle of ∼37 deg. The Gerchberg–Saxton (GS) algorithm [47–49] is used to design the phase profile of the diffuser (see Section S1 of Supplement 1 for details). An optical image of an array of fabricated MDs, each 1.6 mm in diameter, is shown in Fig. 2(e). A scanning electron microscope image of the meta-atoms is shown in Fig. 2(f). Moreover, a gold aperture is deposited around the MDs to block the unwanted light to increase the signal-to-noise ratio (SNR).

3. THEORY AND SIMULATION RESULTS

A. Theory

In linear optical systems, the $\mathbf{T}$ matrix can describe the relationship between an input field (x) and an output field (y) through a linear equation, $y = \mathbf{T}x$. In this section, the properties of the $\mathbf{T}$ matrix of the MD are explored for two reasons. First, knowing $\mathbf{T}$ is a prerequisite of the SSM method, which we utilized to directly retrieve the input complex field x from the output intensity of the speckle pattern, y^*y. Second, the mathematical properties of $\mathbf{T}$ can be utilized not only for better characterization of the MD as a scattering medium, but also to improve our understanding of the operating conditions of the SSM method.

To compute the $\mathbf{T}$ matrix, we performed a numerical study using the designed MD phase mask and the wave propagation method (see Section S1 and Fig. S2 of Supplement 1 for the detailed procedure and the flow graph showing the computation of $\mathbf{T}$). To limit the matrix dimensions and make the calculations manageable in a regular workstation, we limited the input and output space. At the input plane, we limited the object to a 60 × 60 array of 2.5 μm pixels. For each input pixel, the field is then calculated at the output space. After downsampling the output field to compensate for the oversampling caused by the microscope magnification, the effective output space in our system becomes a 210 × 210 array of 1.06 μm pixels (see Section S1 of Supplement 1 for details). Each input/output pixel corresponds to an input/output mode. Therefore, this choice sets the number of input and output modes, N and M, at 3600 and 44,100, respectively. The simulated amplitude and phase of the speckle patterns on the output space for the 1st, 2nd, and Nth input modes are shown in Fig. 3(a).

The calculated complex speckle pattern for the ith input mode, t_i, can be written as an $M \times 1$ vector. This vector then constitutes the ith column of $\mathbf{T}$, which is an $M \times N$ matrix. The SSM, $\mathbf{Z}$, is then computed from $\mathbf{T}$ and the intensity of the speckle pattern resulting from a certain object, y^*y, using [12]

$$Z_{ij} = \frac{1}{\sum_i \sum_j}[\langle t_i^* t_j y^* y\rangle - \langle t_i^* t_j\rangle\langle y^* y\rangle], \tag{1}$$

where $\langle\cdot\rangle$ indicates spatial averaging and $\sum_p = \langle|t_p|^2\rangle$. $\mathbf{Z}$ plays a key role in the complex field retrieval if three conditions are met.

First, the M/N ratio, denoted by Υ, should be much larger than 1. In this case, the rank of $\mathbf{Z}$ becomes one and its eigenvector forms the initial retrieved complex field. In our case Υ is 12.25, which is sufficiently larger than 1, as our system performs well in both simulation and experiment. If a system works well with a low Υ, it is beneficial in terms of computational cost and performance. That's because a low Υ means a wide FOV for a fixed M (i.e., higher performance), or a small-sized $\mathbf{T}$ matrix for a fixed N (i.e., less computation required).

Second, the columns of $\mathbf{T}$ should be orthogonal to each other (i.e., the speckle patterns for different input modes should be uncorrelated). To investigate the orthogonality, we formed a symmetric matrix $\mathbf{G}$ whose elements are the correlation of normalized columns of $\mathbf{T}(G_{ij} = |\langle t_i^* t_j\rangle|/\sqrt{\sum_i \sum_j})$. The elements of $\mathbf{G}$ are plotted in Fig. 3(b), which shows an approximately diagonal matrix with all diagonal elements equal to 1. There are some nonzero off-diagonal elements (with values close to 0.18) corresponding to the speckle field–field correlation between neighboring input modes [50,51]. The correlation drops quickly to negligible amounts for input modes that are farther apart (see Fig. S3 of Supplement 1 for details about the correlation between the columns of $\mathbf{T}$). The almost uncorrelated columns of $\mathbf{T}$ could be explained by the fact that the MD is a subwavelength-thick diffractive layer with a high scattering power. Also, computing the $\mathbf{T}$ matrix avoids additional correlation caused by any type of noise during the experimental characterization procedure. From an engineering viewpoint, it is possible to design the MDs to minimize the correlation between columns of $\mathbf{T}$ for given optical setup conditions. This could be a key advantage of the MD for the purpose of various speckle-based imaging methods based on the $\mathbf{T}$ matrix [5,50]. Nevertheless, as the following numerical and experimental results show, the achieved level of orthogonality works well for the field retrieval. It is also worth noting here that even if the vectors (t_i and t_j) are not orthogonal, one can in principle form and use an orthogonal basis with them using the Gram–Schmidt process [see Figs. S4(a) and S4(b) of Supplement 1 for details].

As the third condition for accurate complex field retrieval, the MD should be designed to scatter light in random directions. To investigate the randomness more rigorously, an eigenvalue analysis of $\mathbf{T}^\dagger\mathbf{T}/M$ was performed, where † denotes the conjugate transpose. It has previously been shown that because of multiple scattering, the distribution of the normalized singular value spectrum of the square $\mathbf{T}$ matrix of a thick CSM follows a quarter-circle law, which is a special case of the Marchenko–Pastur law [50,52,53]. As shown in Fig. 3(c), the distribution of the normalized eigenvalues of $\mathbf{T}^\dagger\mathbf{T}/M$ for the MD deviates from the Marchenko-Pastur law, indicating dependence between the entries of $\mathbf{T}$ [51,54]. This is because unlike with a thick CSM, the MD consists of a single layer of scatterers. Also, the

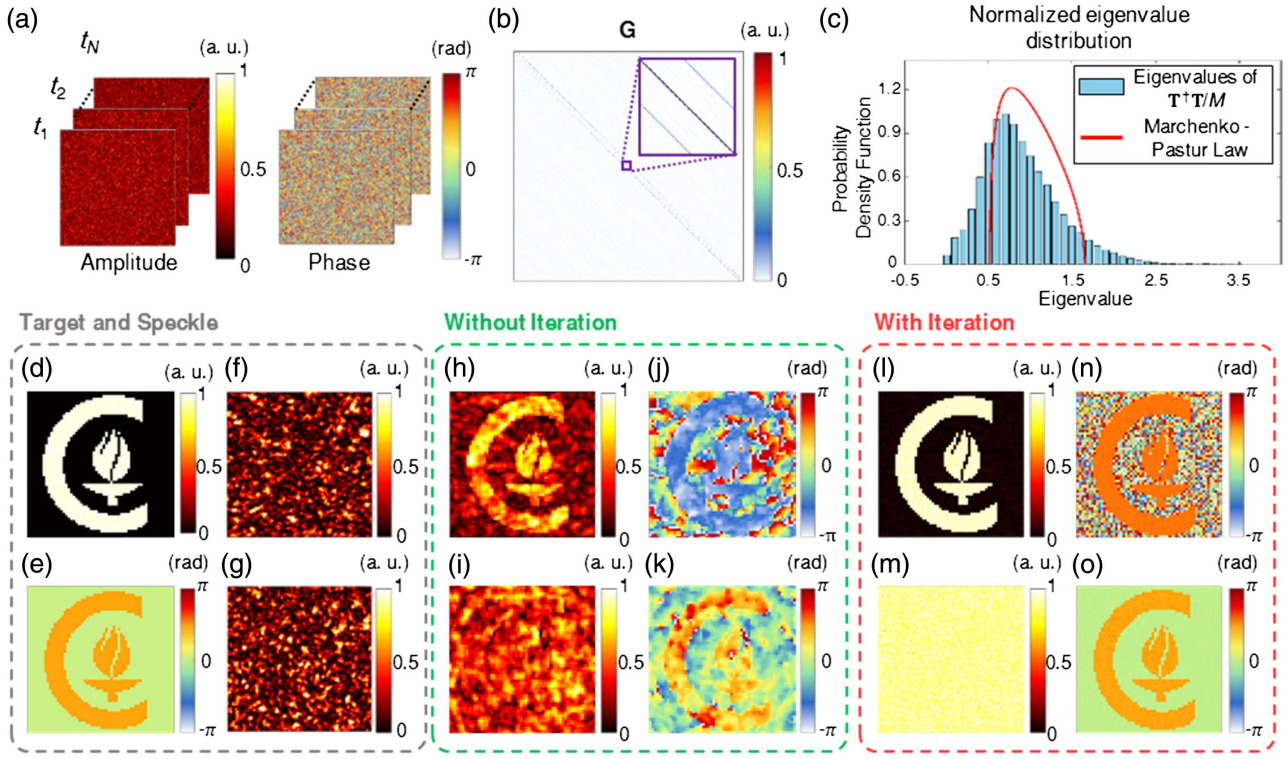

Fig. 3. Numerical investigation of the ability of the MD to retrieve complex fields. (a) Simulated speckle amplitudes and phases for sample input modes, which are then shaped as complex $M \times 1$ vectors and form the columns of $\mathbf{T}$. (b) The $\mathbf{G}$ matrix formed from the inner product mapping of the normalized vectors of $\mathbf{T}$. G_{ij} represents the absolute value of the inner product of normalized t_i and t_j. The 130×130 elements located at the center of $\mathbf{G}$ are magnified in the inset. (c) Eigenvalue distribution of the $\mathbf{T}^\dagger\mathbf{T}/M$ matrix. The solid red line is the Marchenko-Pastur law prediction for a random $M \times N$ matrix. (d), (e) The sample amplitude and phase objects. (f), (g) Simulated speckle patterns of the amplitude and phase objects. (h)–(k) Amplitude and phase maps of the initially retrieved complex fields. (h), (j) Amplitude object. (i), (k) Retrieved fields for the phase object. (l)–(o) Amplitude and phase maps of the retrieved complex fields after 20 iterations.

dependence between the entries is consistent with a large memory-effect range for the MD [25]. However, our experimental and numerical results verify that this level of randomness is enough to implement the SSM method.

B. Simulation Results

To numerically investigate the operation of the MD, we performed simulations using amplitude and phase samples. Figures 3(d) and 3(e) show sample amplitude and phase objects, respectively, along with their corresponding simulated speckle patterns [Figs. 3(f) and 3(g), respectively]. Using the speckle patterns and the precalculated $\mathbf{T}$ matrix, the $\mathbf{Z}$ matrix is calculated for each speckle pattern. The first estimate of the complex field is the eigenvector of $\mathbf{Z}$ corresponding to the eigenvalue with the largest absolute value. The amplitude and phase of these initial estimated fields are shown in Figs. 3(h) and 3(j), respectively, for the amplitude object in Fig. 3(d), and in Figs. 3(i) and 3(k) for the phase object in Fig. 3(e). An iteration method based on the modified GS algorithm (originally proposed by Lee and Park [12]) is then applied to improve the SNR (see Section 1 of Supplement 1 for the detailed computational procedure). The results after 20 iterations are shown in Figs. 3(l)–3(o), demonstrating the ability of the MD to retrieve the complex fields very accurately. Furthermore, to investigate the effects of the orthogonality between the columns of $\mathbf{T}$, we also performed the complex field retrieval of the same amplitude and phase targets with the transmission matrix modified through the Gram–Schmidt process ($\mathbf{T}_{\mathrm{GRAM}}$). We couldn't discern any noticeable difference between the fields retrieved using either matrix, and therefore we conclude that the achieved level of orthogonality is high enough to allow near-ideal operation of the SSM method [see Figs. S4(c)–S4(f) of Supplement 1 for details]. The iteration process converged quickly, showing negligible changes after 20 iterations. Therefore, we used the same number of iterations (20) in the experimental studies as well. On average, calculating the initial retrieved fields and performing the 20 iterations takes less than 30 s in total on our workstation (Intel Xeon E5-2640 CPU; 96.0 Gbytes RAM). Most of the computation time is consumed by multiplication of the large matrices, and thus we expect that the time would significantly decrease with parallel computing.

4. EXPERIMENTAL RESULTS AND FURTHER NUMERICAL ANALYSIS

A. Experimental Complex Field Retrieval with Amplitude Targets

To experimentally test the MD and the method, we use two different parts of the 1951 USAF resolution test target as amplitude objects in the measurement setup shown in Fig. S5(a) of Supplement 1. Figures 4(a) and 4(b) show images of the amplitude objects captured using the conventional microscope (i.e., with the MD and the polarizers removed). The speckle patterns generated by the objects through the MD are plotted in Figs. 4(c) and 4(d). Then, proper downsampling of the speckle pattern is

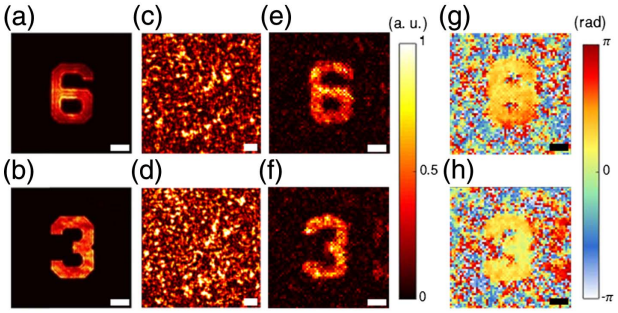

Fig. 4. Experimental retrieval of amplitude objects: (a), (b) in-focus images of targets captured by a custom-built microscope; (c), (d) the resulting speckle patterns of the samples after passing through the MD; (e), (f) the retrieved object amplitudes; (g), (h) phases from the captured speckle patterns. The scale bars are 25 μm.

performed to compensate the oversampling caused by the microscope magnification and image sensor pixel size. The **Z** matrix can then be computed via Eq. (1) using the downsampled speckle intensity patterns and the precalculated **T** matrix. The retrieved amplitudes and phases of the two amplitude objects are shown in Figs. 4(e)–4(h) after 20 iterations [see Figs. S5(b) and S5(c) of Supplement 1 for the retrieved fields before performing iterations].

Unlike with CSM, changing the measurement setup or the input/output mode conditions (distances, pixel sizes and numbers, etc.) does not require the MD to be characterized again. Instead, the new **T** matrix is calculated using the designed phase mask and the new conditions. To examine the reproducibility of the results under such changes, further measurements were performed with different distances and pixel sizes. We were able to reproduce the results under various conditions by just updating the **T** matrix accordingly (see Fig. S6 of Supplement 1 for details). Moreover, the retrieval process is successful despite the experimental noise. To show the effect of a large Υ, we also performed the complex field retrieval for a Υ value of 69.4. The large Υ results in improved accuracy of the initial retrievals and retrievals after 20 iterations, as well as in an increased computation time from 30 s to 3 min on average (see Fig. S7 of Supplement 1 for details). In addition, the optical properties of the MD are stable over time, and no noticeable change was observed in more than five months. It is also worth noting here that a thin linear polarizer and a compact image sensor can replace the custom-built microscope for miniaturization.

B. Numerical Noise Tolerance Analysis

We performed a numerical noise tolerance study using the computed **T** matrix of the MD. Various intensity noises with a Gaussian distribution and different energies were added numerically to the simulated and measured speckle intensity patterns to adjust the SNR. We focused on incoherent intensity noise, because the employed cross-polarized scheme cuts almost all of the coherent noise from the laser. The results of the noise tolerance study are summarized in Fig. 5. First, we investigated the noise tolerance with the calculated speckle intensity patterns. The initially retrieved fields for various SNR values are plotted in Figs. 5(a) and 5(b) for an amplitude object, and Figs. 5(c) and 5(d) for a phase object. The retrieval process works for SNR values greater than 1, and the initially retrieved fields look almost identical for SNR values larger than 5. Figures 5(e)–5(h)

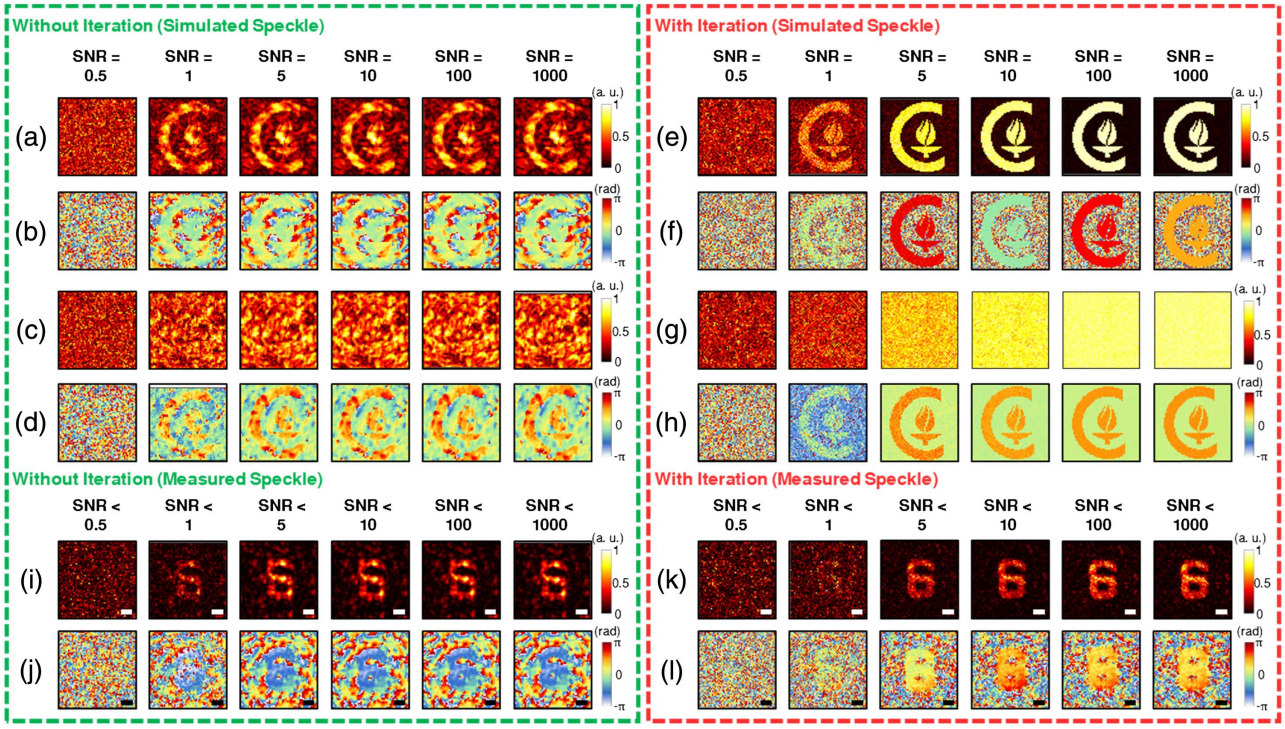

Fig. 5. Numerical noise tolerance analysis. (a)–(d) Retrieved amplitudes and phases for the amplitude and phase objects in Figs. 3(d) and 3(e) for SNR values from 0.5 to 1000. A Gaussian noise is added to the simulated speckle patterns to test the noise tolerance. (e)–(h) Reconstructed objects after performing 20 iterations of the GS algorithm using the results in (a)–(d) as initial points. (i), (j) Retrieved intensity and phase maps for the object shown in Fig. 4(a) when changing the SNR from 0.5 to 1000. A Gaussian noise is added to the measured speckle pattern shown in Fig. 4(c). (k), (l) Reconstructed intensity and phase maps after conducting 20 iterations of the GS algorithm using (i) and (j). The scale bars in (i)–(l) are 25 μm.

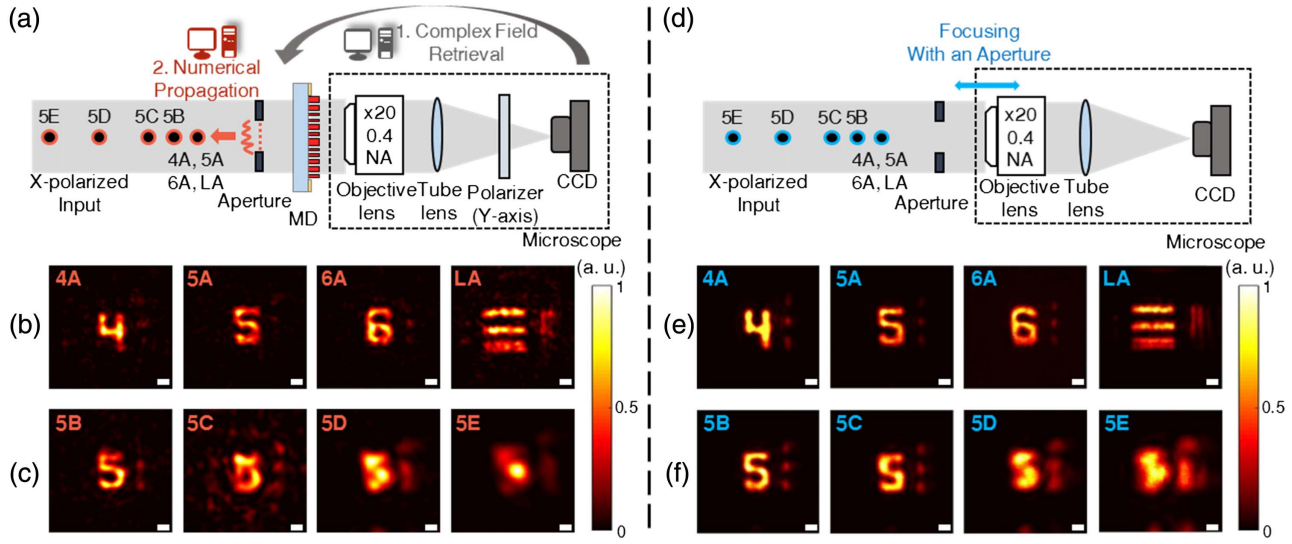

Fig. 6. Experimental results of complex field retrieval for holographic imaging. (a) Schematic drawing of the measurement setup showing the computational steps. The complex field is retrieved at the 150 μm aperture using the captured speckle pattern. The field is then backpropagated to reconstruct the object at different distances from the aperture. (b) Reconstructed images for different objects at point A. (c) Reconstructed images for a target shaped like the number 5 at different distances from the aperture. (d) Schematic drawing of a microscope setup that images the target through the same aperture for comparison. (e) Captured in-focus images with the microscope for the same objects as in (b). (f) Captured in-focus images with the microscope for the same object and distances as in (c). The distances between the points and the aperture are as follows: A, 1.5 mm; B, 2 mm; C, 2.5 mm; D, 3.5 mm; and E, 4.5 mm. Scale bars are 25 μm.

show the retrieved fields after 20 iterations. As expected, the retrieval accuracy improves as the SNR value increases. The same analysis can be performed using the measured speckle patterns. To this end, the Gaussian intensity noise was numerically added to the experimentally measured speckle pattern shown in Fig. 4(c). We should note here that the actual SNR value of the *noisy* speckle pattern is less than the numerically controlled SNR, since the measured speckle pattern already includes the measurement noise and errors arising from imperfections in the fabricated MD. The results shown in Figs. 5(i)–5(l) are comparable to the amplitude target shown in Fig. 4(a). If the SNR is less than 1, it is better to avoid iterations, since the iteration process automatically assumes a high SNR in the speckle pattern.

It is worth noting the differences between the noise tolerance analysis in this work and the study performed by Lee and Park [12]. Here, we used the computed transfer matrix of the actual MD instead of the randomly generated complex matrix used in [12]. The randomly generated transfer matrix has almost perfectly uncorrelated columns, and its corresponding eigenvalue spectrum follows the Marchenko–Pastur law (i.e., it is almost ideal for the SSM method). Nevertheless, our results for the MD show better noise tolerance and similar retrieval performance in comparison to the randomly generated transfer matrix (see Section S2 and Fig. S8 of Supplement 1 for details). In addition, here the noise tolerance was investigated using both simulated and measured speckle patterns, and we observed that the complex fields can be retrieved in both cases, even for a low Υ value of 12.25 and an SNR value as low as 1.

C. Holographic Imaging Experiment and Numerical Analysis of Robustness against Misalignment

To further demonstrate the ability of the MD and the method to retrieve complex fields, we performed holographic imaging experiments. To this end, the complex fields are retrieved at a 150 μm aperture behind the MD [Fig. 6(a)]. The fields are then numerically backpropagated to the desired distance to reconstruct the object behind the aperture. We imaged several target objects at different distances from the aperture, as shown in Fig. 6(a). The reconstructed objects are shown in Figs. 6(b) and 6(c) for different targets and distances. For comparison, we also imaged the objects through the same aperture using the microscope shown in Fig. 6(d). The results are plotted in Figs. 6(e) and 6(f), showing good agreement with the MD results. The retrieved complex fields for all images at the aperture are shown in Fig. S9 of Supplement 1. In both Figs. 6(c) and 6(f), the image resolution decreases as the object distance to the aperture increases. This is due to the smaller effective NA of the system in imaging farther objects as the aperture diameter is kept constant. We also numerically investigated the performance of the MD and the method under axial and transverse misalignments. Not only is the method robust to the MD displacement in the axial and transverse directions, but also some misalignments can be corrected or exploited in the alignment of the optical system (see Section S3 and Fig. S10 of Supplement 1 for details).

5. DISCUSSION AND CONCLUSION

In summary, we demonstrated computational complex field imaging using dielectric MDs. We investigated the mathematical properties of the $\mathbf{T}$ matrix of the MD and demonstrated its performance as a scattering medium in the SSM method. In addition, we discussed the advantages of MDs for computational imaging over the CSM. A key benefit is the replacement of the difficult and time-consuming characterization process with a single simulation. The MD provides reliable reproducibility, long-term stability, high noise tolerance even for small Υ values,

and robustness against misalignments. CSM usually suffer from the trade-off between the light efficiency and maximum scattering angle, because both are highly dependent on the thickness of the CSM. In contrast, the MD can achieve high transmission and a large maximum scattering angle at the same time. This could be a noteworthy property for future investigations based on the MDs. Another important property of the MDs is the possibility of mass-producing designed MDs with almost identical optical properties. Avoiding the required case-by-case characterization could be a key factor in applying scattering-medium-based computational imaging techniques in real-life applications.

Similar to some other lensless techniques, speckle-based computational imaging systems can overcome some of the limits of conventional lens-based imaging systems, such as the trade-off between resolution and FOV [55]. In addition, it is worth noting that the lensless imaging systems inherently suffer less from various monochromatic and chromatic optical aberrations, which are major challenges faced by metasurface lenses [56–62]. Even though the relatively heavy computational load is generally one of the main drawbacks for computational imaging systems, recent investigations based on deep learning have shown not only a significant decrease in the computational load but also improved imaging performance [63–65].

This work can be extended to various existing speckle-based computational optics schemes and may be beneficial for a diverse set of applications. For example, endoscopes for *in vivo* quantitative phase imaging can be realized by using the MD and thin linear polarizers in existing image-sensor-based endoscopes with a laser light source [66–68]. Due to the compactness of the MD and its compatibility with semiconductor fabrication processes, it might be possible to integrate the MD-based holographic camera into smartphones or other electronic devices for the purpose of point-of-care diagnostics [69] and holography [70]. Furthermore, we expect that the versatile metasurface platform, which enables scattering media with tailored properties, can be exploited for speckle-based optical encryption [71,72].

Funding. Caltech Innovation Initiative.

Acknowledgment. We thank Babak Hassibi, Changhuei Yang, and Juhyun Kim for helpful discussion. We greatly appreciate the critical support and infrastructure provided for this work by the Kavli Nanoscience Institute at Caltech.

See Supplement 1 for supporting content.

REFERENCES

1. D. Huang, E. A. Swanson, C. P. Lin, J. S. Schuman, W. G. Stinson, W. Chang, M. R. Hee, T. Flotte, K. Gregory, and C. A. Puliafito, "Optical coherence tomography," Science **254**, 1178–1181 (1991).
2. R. Horstmeyer, H. Ruan, and C. Yang, "Guidestar-assisted wavefront-shaping methods for focusing light into biological tissue," Nat. Photonics **9**, 563–571 (2015).
3. J. Bertolotti, E. G. van Putten, C. Blum, A. Lagendijk, W. L. Vos, and A. P. Mosk, "Non-invasive imaging through opaque scattering layers," Nature **491**, 232–234 (2012).
4. O. Katz, P. Heidmann, M. Fink, and S. Gigan, "Non-invasive single-shot imaging through scattering layers and around corners via speckle correlations," Nat. Photonics **8**, 784–790 (2014).
5. S. Popoff, G. Lerosey, M. Fink, A. C. Boccara, and S. Gigan, "Image transmission through an opaque material," Nat. Commun. **1**, 81 (2010).
6. K. T. Takasaki and J. W. Fleischer, "Phase-space measurement for depth-resolved memory-effect imaging," Opt. Express **22**, 31426–31433 (2014).
7. H.-Y. Liu, E. Jonas, L. Tian, J. Zhong, B. Recht, and L. Waller, "3D imaging in volumetric scattering media using phase-space measurements," Opt. Express **23**, 14461–14471 (2015).
8. A. Singh, D. Naik, G. Pedrini, M. Takeda, and W. Osten, "Exploiting scattering media for exploring 3D objects," Light Sci. Appl. **6**, e16219 (2017).
9. R. Horisaki, R. Egami, and J. Tanida, "Single-shot phase imaging with randomized light (SPIRaL)," Opt. Express **24**, 3765–3773 (2016).
10. N. Antipa, G. Kuo, R. Heckel, B. Mildenhall, E. Bostan, R. Ng, and L. Waller, "DiffuserCam: lensless single-exposure 3D imaging," Optica **5**, 1–9 (2018).
11. X. Xie, H. Zhuang, H. He, X. Xu, H. Liang, Y. Liu, and J. Zhou, "Extended depth-resolved imaging through a thin scattering medium with PSF manipulation," Sci. Rep. **8**, 4585 (2018).
12. K. Lee and Y. Park, "Exploiting the speckle-correlation scattering matrix for a compact reference-free holographic image sensor," Nat. Commun. **7**, 13359 (2016).
13. Y. Baek, K. Lee, and Y. Park, "High-resolution long-working-distance reference-free holographic microscopy exploiting speckle-correlation scattering matrix," arXiv: 1802.10321 (2018).
14. P. Berto, H. Rigneault, and M. Guillon, "Wavefront sensing with a thin diffuser," Opt. Lett. **42**, 5117–5120 (2017).
15. B. Redding, S. F. Liew, R. Sarma, and H. Cao, "Compact spectrometer based on a disordered photonic chip," Nat. Photonics **7**, 746–751 (2013).
16. M. Chakrabarti, M. L. Jakobsen, and S. G. Hanson, "Speckle-based spectrometer," Opt. Lett. **40**, 3264–3267 (2015).
17. M. Mazilu, T. Vettenburg, A. Di Falco, and K. Dholakia, "Random superprism wavelength meter," Opt. Lett. **39**, 96–99 (2014).
18. S. Sahoo, D. Tang, and C. Dang, "Single-shot multispectral imaging with a monochromatic camera," Optica **4**, 1209–1213 (2017).
19. K. Lee and Y. Park, "Direct measurements of quantum states by exploiting diffused photon state," arXiv: 1709.08844 (2017).
20. L. Gong, Q. Zhao, H. Zhang, X. Hu, and Y. Li, "Exploiting scattering for single-shot measurement of the orbital angular momentum spectrum of light fields," Proc. SPIE **10712**, 107121F (2018).
21. H. Yilmaz, E. G. van Putten, J. Bertolotti, A. Lagendijk, W. L. Vos, and A. P. Mosk, "Speckle correlation resolution enhancement of wide-field fluorescence imaging," Optica **2**, 424–429 (2015).
22. Y. Kashter, A. Vijayakumar, and J. Rosen, "Resolving images by blurring: superresolution method with a scattering mask between the observed objects and the hologram recorder," Optica **4**, 932–939 (2017).
23. I. M. Vellekoop and A. P. Mosk, "Focusing coherent light through opaque strongly scattering media," Opt. Lett. **32**, 2309–2311 (2007).
24. A. Goetschy and A. D. Stone, "Filtering random matrices: the effect of incomplete channel control in multiple scattering," Phys. Rev. Lett. **111**, 063901 (2013).
25. M. Jang, Y. Horie, A. Shibukawa, J. Brake, Y. Liu, S. M. Kamali, A. Arbabi, H. Ruan, A. Faraon, and C. Yang, "Wavefront shaping with disorder-engineered metasurfaces," Nat. Photonics **12**, 84–90 (2018).
26. N. Yu and F. Capasso, "Flat optics with designer metasurfaces," Nat. Mater. **13**, 139–150 (2014).
27. S. Jahani and Z. Jacob, "All-dielectric metamaterials," Nat. Nanotechnol. **11**, 23–36 (2016).
28. F. Ding, A. Pors, and S. I. Bozhevolnyi, "Gradient metasurfaces: a review of fundamentals and applications," Rep. Prog. Phys. **81**, 026401 (2018).
29. H. H. Hsiao, C. H. Chu, and D. P. Tsai, "Fundamentals and applications of metasurfaces," Small Methods **1**, 1600064 (2017).
30. P. Genevet, F. Capasso, F. Aieta, M. Khorasaninejad, and R. Devlin, "Recent advances in planar optics: from plasmonic to dielectric metasurfaces," Optica **4**, 139–152 (2017).
31. Y. F. Yu, A. Y. Zhu, R. Paniagua-Domínguez, Y. H. Fu, B. Luk'yanchuk, and A. I. Kuznetsov, "High-transmission dielectric metasurface with 2π phase control at visible wavelengths," Laser Photon. Rev. **9**, 412–418 (2015).
32. P. Moitra, B. A. Slovick, W. Li, I. I. Kravchencko, D. P. Briggs, S. Krishnamurthy, and J. Valentine, "Large-scale all-dielectric metamaterial perfect reflectors," ACS Photon. **2**, 692–698 (2015).
33. A. Arbabi, Y. Horie, A. J. Ball, M. Bagheri, and A. Faraon, "Subwavelength-thick lenses with high numerical apertures and large efficiency based on high-contrast transmitarrays," Nat. Commun. **6**, 7069 (2015).

34. M. Khorasaninejad, W. T. Chen, R. C. Devlin, J. Oh, A. Y. Zhu, and F. Capasso, "Metalenses at visible wavelengths: diffraction-limited focusing and subwavelength resolution imaging," Science **352**, 1190–1194 (2016).
35. L. Wang, S. Kruk, H. Tang, T. Li, I. Kravchenko, D. N. Neshev, and Y. S. Kivshar, "Grayscale transparent metasurface holograms," Optica **3**, 1504–1505 (2016).
36. S. M. Kamali, A. Arbabi, E. Arbabi, Y. Horie, and A. Faraon, "Decoupling optical function and geometrical form using conformal flexible dielectric metasurfaces," Nat. Commun. **7**, 11618 (2016).
37. A. Arbabi, E. Arbabi, Y. Horie, S. M. Kamali, and A. Faraon, "Planar metasurface retroreflector," Nat. Photonics **11**, 415–420 (2017).
38. S. Colburn, A. Zhan, and A. Majumdar, "Metasurface optics for full-color computational imaging," Sci. Adv. **4**, eaar2114 (2018).
39. H. C. Liu, B. Yang, Q. Guo, J. Shi, C. Guan, G. Zheng, H. Mühlenbernd, G. Li, T. Zentgraf, and S. Zhang, "Single-pixel computational ghost imaging with helicity-dependent metasurface hologram," Sci. Adv. **3**, e1701477 (2017).
40. A. Pors, F. Ding, Y. Chen, I. P. Radko, and S. I. Bozhevolnyi, "Random-phase metasurfaces at optical wavelengths," Sci. Rep. **6**, 28448 (2016).
41. M. Castro-Lopez, M. Gaio, S. Sellers, G. Gkantzounis, M. Florescu, and R. Sapienza, "Reciprocal space engineering with hyperuniform gold metasurfaces," APL Photon. **2**, 061302 (2017).
42. E. Maguid, M. Yannai, A. Faerman, I. Yulevich, V. Kleiner, and E. Hasman, "Disorder-induced optical transition from spin Hall to random Rashba effect," Science **358**, 1411–1415 (2017).
43. M. S. Asif, A. Ayremlou, A. Veeraraghavan, R. Baraniuk, and A. Sankaranarayanan, "FlatCam: replacing lenses with masks and computation," in *IEEE International Conference on Computer Vision Workshop (ICCVW)* (IEEE, 2015), pp. 663–666.
44. R. Horisaki, R. Egami, and J. Tanida, "Experimental demonstration of single-shot phase imaging with a coded aperture," Opt. Express **23**, 28691–28697 (2015).
45. J. K. Adams, V. Boominathan, B. W. Avants, D. G. Vercosa, F. Ye, R. G. Baraniuk, J. T. Robinson, and A. Veeraraghavan, "Single-frame 3D fluorescence microscopy with ultraminiature lensless FlatScope," Sci. Adv. **3**, e1701548 (2017).
46. A. Arbabi, Y. Horie, M. Bagheri, and A. Faraon, "Dielectric metasurfaces for complete control of phase and polarization with subwavelength spatial resolution and high transmission," Nat. Nanotechnol. **10**, 937–943 (2015).
47. R. W. Gerchberg and W. O. Saxton, "A practical algorithm for the determination of the phase from image and diffraction plane pictures," Optik **35**, 237–246 (1972).
48. J. R. Fienup, "Phase retrieval algorithms: a comparison," Appl. Opt. **21**, 2758–2769 (1982).
49. R. Piestun, B. Spektor, and J. Shamir, "Wave fields in three dimensions: analysis and synthesis," J. Opt. Soc. Am. A **13**, 1837–1848 (1996).
50. S. M. Popoff, G. Lerosey, R. Carminati, M. Fink, A. C. Boccara, and S. Gigan, "Measuring the transmission matrix in optics: an approach to the study and control of light propagation in disordered media," Phys. Rev. Lett. **104**, 100601 (2010).
51. C. W. Hsu, S. F. Liew, A. Goetschy, H. Cao, and A. D. Stone, "Correlation-enhanced control of wave focusing in disordered media," Nat. Phys. **13**, 497–502 (2017).
52. S. M. Popoff, G. Lerosey, M. Fink, A. C. Boccara, and S. Gigan, "Controlling light through optical disordered media: transmission matrix approach," New J. Phys. **13**, 123021 (2011).
53. V. A. Marčenko and L. A. Pastur, "Distribution of eigenvalues for some sets of random matrices," Math. USSR **1**, 457–483 (1967).
54. H. Yu, T. R. Hillman, W. Choi, J. O. Lee, M. S. Feld, R. R. Dasari, and Y. Park, "Measuring large optical transmission matrices of disordered media," Phys. Rev. Lett. **111**, 153902 (2013).
55. A. Greenbaum, W. Luo, T.-W. Su, Z. Göröcs, L. Xue, S. O. Isikman, A. F. Coskun, O. Mudanyali, and A. Ozcan, "Imaging without lenses: achievements and remaining challenges of wide-field on-chip microscopy," Nat. Methods **9**, 889–895 (2012).
56. A. Arbabi, E. Arbabi, S. M. Kamali, Y. Horie, S. Han, and A. Faraon, "Miniature optical planar camera based on a wide-angle metasurface doublet corrected for monochromatic aberrations," Nat. Commun. **7**, 13682 (2016).
57. B. Groever, W. T. Chen, and F. Capasso, "Meta-lens doublet in the visible region," Nano Lett. **17**, 4902–4907 (2017).
58. F. Aieta, M. A. Kats, P. Genevet, and F. Capasso, "Multiwavelength achromatic metasurfaces by dispersive phase compensation," Science **347**, 1342–1345 (2015).
59. E. Arbabi, A. Arbabi, S. M. Kamali, Y. Horie, and A. Faraon, "Controlling the sign of chromatic dispersion in diffractive optics," Optica **4**, 625–632 (2017).
60. W. T. Chen, A. Y. Zhu, V. Sanjeev, M. Khorasaninejad, Z. Shi, E. Lee, and F. Capasso, "A broadband achromatic metalens for focusing and imaging in the visible," Nat. Nanotechnol. **13**, 220–226 (2018).
61. S. Wang, P. C. Wu, V.-C. Su, Y.-C. Lai, M.-K. Chen, H. Y. Kuo, B. H. Chen, Y. H. Chen, T.-T. Huang, J.-H. Wang, R.-M. Lin, C.-H. Kuan, T. Li, Z. Wang, S. Zhu, and D. P. Tsai, "A broadband achromatic metalens in the visible," Nat. Nanotechnol. **13**, 227–232 (2018).
62. S. Wang, P. C. Wu, V.-C. Su, Y.-C. Lai, C. H. Chu, J.-W. Chen, S.-H. Lu, J. Chen, B. Xu, C.-H. Kuan, T. Li, S. Zhu, and D. P. Tsai, "Broadband achromatic optical metasurface devices," Nat. Commun. **8**, 187 (2017).
63. A. Sinha, J. Lee, S. Li, and G. Barbastathis, "Lensless computational imaging through deep learning," Optica **4**, 1117–1125 (2017).
64. Y. Rivenson, Y. Zhang, H. Günaydın, D. Teng, and A. Ozcan, "Phase recovery and holographic image reconstruction using deep learning in neural networks," Light Sci. Appl. **7**, 17141 (2018).
65. Y. Wu, Y. Rivenson, Y. Zhang, Z. Wei, H. Günaydin, X. Lin, and A. Ozcan, "Extended depth-of-field in holographic imaging using deep-learning-based autofocusing and phase recovery," Optica **5**, 704–710 (2018).
66. G. Popescu, *Quantitative Phase Imaging of Cells and Tissues* (McGraw-Hill, 2011).
67. K. Lee, K. Kim, J. Jung, J. H. Heo, S. Cho, S. Lee, G. Chang, Y. J. Jo, H. Park, and Y. K. Park, "Quantitative phase imaging techniques for the study of cell pathophysiology: from principles to applications," Sensors **13**, 4170–4191 (2013).
68. H. Lee, Y. Lee, C. Song, H. R. Cho, R. Ghaffari, T. K. Choi, K. H. Kim, Y. B. Lee, D. Ling, H. Lee, S. J. Yu, S. H. Choi, T. Hyeon, and D. H. Kim, "An endoscope with integrated transparent bioelectronics and theranostic nanoparticles for colon cancer treatment," Nat. Commun. **6**, 10059 (2015).
69. H. Zhu, S. O. Isikman, O. Mudanyali, A. Greenbaum, and A. Ozcan, "Optical imaging techniques for point-of-care diagnostics," Lab Chip **13**, 51–67 (2013).
70. D. Gabor, "A new microscopic principle," Nature **161**, 777–778 (1948).
71. R. Pappu, B. Recht, J. Taylor, and N. Gershenfeld, "Physical one-way functions," Science **297**, 2026–2030 (2002).
72. R. Horstmeyer, B. Judkewitz, I. M. Vellekoop, S. Assawaworrarit, and C. Yang, "Physical key-protected one-time pad," Sci. Rep. **3**, 3543 (2013).